Journal of Advances in Chemical Sciences
ISSN 3121-6730
Volume 3, Number 1, 2026

Synthesis and Characterisation of Iron Oxide Nanoparticles Supported on Modified Maize Stalk for the Remediation of Congo Red and Methyl Orange from Wastewater

[*1, 2]Nafiu Muhammad, [1]Yau Mohammed, [1]Kabir Ado, and [1]P. E. Umoru

[1]Chemistry Department, Faculty of Science,

Nigerian Defence Academy, Kaduna, Nigeria.

[2]Department of Pure and Industrial chemistry, Faculty of Natural and Applied Sciences,

Umaru Musa Yar'dau University, Katsina, Nigeria

*Corresponding Author: nafiu.muhammad@umyu.edu.ng

Received 2nd June**,** 2026 **Accepted** 24th July, 2026, **Published online** 4th August, 2026

Abstract

This study developed a sustainable composite of iron nanoparticles supported on modified maize stalk (FeNps/MMS) for wastewater treatment. The nanoparticles were synthesized via microwave-assisted co-precipitation and subsequently loaded onto chemically modified maize stalk biomass. Characterization employing FTIR, SEM, XRD, and BET confirmed successful composite fabrication, revealing an average crystallite size of approximately 52 nm, a high specific surface area of 249.9 $m^2\ g^{-1}$, and a well-developed micro-mesoporous structure. The FeNps/MMS composite exhibited outstanding removal performance for the azo dyes Congo Red and Methyl Orange, achieving efficiencies of 90% and 86%, with corresponding equilibrium adsorption capacities of 7.23 mg g^{-1} and 7.13 mg g^{-1}, respectively. Kinetic studies showed that adsorption adhered to the pseudo-second-order model, suggesting that the process was primarily governed by surface interactions. Equilibrium data were well-represented by the Freundlich isotherm (R^2 = 0.9588 for Congo Red and 0.9953 for Methyl Orange), indicative of multilayer adsorption onto heterogeneous surfaces. Moreover, mean adsorption energies derived from the Dubinin–Radushkevich model (5.16 kJ mol^{-1} and 5.79 kJ mol^{-1}) confirmed the dominant role of physical adsorption. Thermodynamic evaluations indicated that Congo Red adsorption was spontaneous and endothermic, whereas Methyl Orange adsorption was spontaneous and exothermic. Importantly, the composite retained substantial removal efficiency across repeated adsorption-desorption cycles, evidencing excellent stability and reusability. These findings indicate that FeNps/MMS is an efficient, reusable, and environmentally friendly adsorbent for dye-contaminated wastewater treatment.

Keywords: FeNps-composite, Dye adsorption, wastewater remediation

Introduction

The contamination of water resources by industrial effluents has become a major environmental problem, posing serious risks to aquatic ecosystems and human health [1–3]. Among the most persistent pollutants are synthetic azo dyes, particularly Congo Red and Methyl Orange, which are widely used in the textile, paper, leather, and printing industries [4, 5]. The discharge of these dyes into water bodies causes intense colouration, reduces light penetration, inhibits photosynthesis, and may produce toxic, mutagenic, and carcinogenic aromatic amines during degradation [4–7]. Their complex aromatic structures and high chemical stability make them resistant to conventional biological and physicochemical wastewater treatment processes, creating the need for efficient and sustainable remediation technologies [4–7].

The control of these pollutants in wastewater is not only an environmental necessity but also a legal requirement in many countries [4]. Environmental regulatory agencies have established strict discharge limits for these pollutants before industrial effluents are released into natural water bodies. However, compliance remains a major challenge, particularly in developing countries where wastewater treatment infrastructure is inadequate or treatment costs are prohibitively high [4–7]. Conventional treatment technologies, including chemical precipitation, coagulation–flocculation, ion exchange, membrane filtration, and advanced oxidation processes, are capable of removing selected contaminants but are often expensive, energy-intensive, and less effective at low pollutant concentrations [2]. In addition, many of these technologies produce secondary waste streams, such as sludge, which require further treatment and safe disposal [2,3]

Adsorption is one of the most effective methods for removing dye pollutants because of its simplicity, high removal efficiency, low operating cost, and ease of operation [8, 9]. However, the success of adsorption depends largely on the characteristics of the adsorbent. Iron oxide nanoparticles have attracted considerable attention because of their high specific surface area, abundant active sites, magnetic properties, and excellent adsorption capacity [9–11]. Despite these advantages, their practical application is limited by particle aggregation, poor stability, difficult recovery after use, and reduced adsorption performance caused by their high surface energy [9–12]. To overcome these limitations, FeNps are commonly immobilized on porous support materials that improve their stability, dispersion, and reusability.

Agricultural residues have emerged as promising support materials because they are renewable, inexpensive, biodegradable, and rich in lignocellulosic components containing hydroxyl and

carboxyl functional groups [13, 14]. These functional groups provide active sites for nanoparticle anchoring and pollutant adsorption [19, 20]. Consequently, agricultural wastes such as rice husks, sugarcane bagasse, coconut shells, and peanut shells, have been investigated as supports for nanoparticle-based adsorbents [18–20] The resulting composites combine the high adsorption capacity of iron oxide nanoparticles with the porous structure, mechanical stability, and surface functionality of biomass, thereby reducing nanoparticle aggregation and improving adsorption efficiency [19, 20].

Although iron oxide nanoparticle-biomass composites have been widely investigated for wastewater treatment, most have been synthesized using conventional methods such as hydrothermal, thermal, or ultrasonic techniques [21]. The combined use of chemical modification and microwave-assisted synthesis to fabricate iron oxide nanoparticle composites supported on maize stalk has received limited attention, particularly for the removal of Congo Red and Methyl Orange. Furthermore, the influence of this synthesis approach on the structural properties, adsorption behaviour, thermodynamic characteristics, and regeneration performance of the resulting composites remains insufficiently understood. Therefore, there is a need to develop and comprehensively evaluate a stable, low-cost, and environmentally friendly adsorbent based on this abundant agricultural residue for efficient dye removal from wastewater.

This study was undertaken to address these knowledge gaps by developing iron oxide nanoparticle composites supported on chemically modified maize stalk. The study integrates microwave-assisted nanomaterial synthesis with agricultural waste valorisation to produce an efficient and reusable adsorbent for wastewater treatment. By optimizing the synthesis conditions, characterizing the physicochemical properties of the composite, and evaluating its adsorption performance under different operating conditions, this work contributes to the development of sustainable, efficient, and affordable technologies for wastewater remediation. The successful development of this material not only provide an effective solution for removing dye pollutants from wastewater but also promote the conversion of agricultural waste into high-value functional materials in line with circular economy principles.

Materials and Methods

Chemicals and Reagents

All chemicals employed were analytical-grade reagents used as received. These included: iron(III) chloride ($FeCl_3$, BDH), iron(II) sulphate heptahydrate ($FeSO_4 \cdot 7H_2O$, Sigma, 99%), sodium hydroxide (NaOH, Sigma, 97%), Hydrochloric acid (BDH), ethanol (C_2H_5OH, BDH,

99.8%), methanol (CH_3OH, BDH, 99.8%), potassium chloride (KCl, BDH, 96%), potassium permanganate ($KMnO_4$, Sigma, 97%), and potassium hydroxide (KOH, Sigma, 97%), Methyl Orange powder ($C_{14}H_{14}N_3NaO_3S$) (Fishser), Congo red dye ($C_{32}H_{22}N_6Na_2O_6S_2$)(sigma)

Instrumentation

Material morphology were examined using a Phenom Pharos G2 Scanning Electron Microscope (thermo Fisher scientific). Functional group analysis was performed on an Agilent Cary 630 Fourier-transform infrared (FTIR) spectrometer. Specific surface area and porosity were measured with a Quantachrome BET surface analyzer. Dye concentrations were determined by UV-VIS (Milton Roy Array 3000). Additional apparatus included a Philips blender (HR2114/05) for biomass homogenization, a Hanna Instruments pH meter, a Hisense microwave oven, a Heraeus Christ Labofuge 1 centrifuge, and a magnetic stirrer.

Biomass Collection and Preparation

Collection of Maize Stalks

Maize stalk samples were collected via grab sampling from Gidangona Farms, located in Katsina State, Nigeria. The specimens were subsequently transported to the Department of Biological Sciences at Umaru Musa Yar'adua University in labelled polyethylene bags, where they were identified and authenticated as *Zea mays L*

Pre-treatment of Biomass

The outer epidermal layers of the maize stalks were manually removed, after which the stalks were cut into smaller pieces and thoroughly washed with double-distilled water. The cleaned material was oven-dried at 105 °C for 20 min, milled into a fine powder (MSP) using Philips blender (HR2114/05), and stored in airtight containers prior to use.

Synthesis of Adsorbents

Iron Nanoparticles (FeNps)

FeNps were synthesized via co-precipitation coupled a microwave-assisted method. About 10 g of $FeCl_3$ and 5 g of $FeSO_4{\cdot}7H_2O$ were homogenized in 100 mL of 20% ethanol for 20 minutes. The solution pH was elevated to 11 via the dropwise addition of 5 M NaOH. The mixture was subjected to microwave irradiation at 60 ^{0}C for 20 minutes. The resulting reddish-brown precipitate was centrifuged (250 rpm), washed with deionized water and ethanol until a neutral pH was achieved, and dried at 80 ℃ [22].

Modified Maize Stalk (MMS)

MSP (5 g) was introduced to 150 mL of 1 M $KMnO_4$ and agitated at 300 rpm for 1 hour. Subsequently, 50 mL of 0.5 M NaOH was integrated slowly. The mixture was microwave-treated at 40 ℃ for 20 minutes and stirred for 10 minutes post-irradiation. The solid phase was recovered via filtration, washed to neutrality, and dried at 40 ℃ to yield MMS.

FeNps/MMS Composite Fabrication

To prepare the composite, 10 g of FeNps were ultrasonically dispersed in 100 mL of 20% ethanol for 30 minutes. Following this, 3 g of MMS and 10 mL of 0.1 M NaOH were added under constant stirring at speed of 150 rpm. The final suspension was processed in a microwave at 50 ℃ for 2 hours. The final FeNps/MMS composite was filtered, washed, and dried at 80 ℃.

Analytical Calibration

Congo red and Methyl orange concentrations were analysed using UV–Visible spectrophotometry at 497 nm and 460 nm respectively. Triplicate measurements were taken for each concentration, and linear regression was applied to establish the calibration equations.

Batch Adsorption Studies

Optimization of Parameters

Batch experiments were conducted in 50 mL adsorbate solutions. Variables including adsorbent dose (20–120 mg), solution pH (3–11), initial metal concentration (2–10 mg L^{-1}), contact time (5–40 min), and temperature (300–320 K) optimized under constant agitation (200 rpm). Residual dye concentrations were quantified by UV-VIS.

Adsorption Capacity and Efficiency

The adsorption capacity at equilibrium (q_e, mg g^{-1}) and percentage removal were computed using equations 1 and 2:

$$q_e = \frac{(C_0 - C_e)V}{W} \quad (1)$$

$$Removal\ \% = \frac{(C_0 - C_e)}{W} X100 \quad (2)$$

Where C_0 and C_e (mg L^{-1}) are the initial and equilibrium concentrations, V (L) is the solution volume, and W (g) is the adsorbent mass.

Adsorption Modelling and Thermodynamics

Adsorption kinetics and isotherms

Adsorption kinetics were investigated to understand the uptake mechanism and rate-controlling steps using the pseudo-first-order (PFO), pseudo-second-order (PSO), Elovich, and intraparticle diffusion models. The PFO model is expressed as

$$\ln(q_e - q_t) = lnq_e - k_1 t \quad (3)$$

Where qe and qt (mg/g) are the amounts adsorbed at equilibrium and at time (t) (min), respectively, and k_1 (min^{-1}) is the rate constant. The PSO model is given by

$$\frac{t}{q_t} = \frac{1}{k_2 q_e^2} + \frac{t}{q_e} \quad (4)$$

where k_2 (g mg^{-1} min^{-1}) is the PSO rate constant, obtained from the slope and intercept of the t/qt versus t plot. The Elovich equation is written as

$$q_t = \frac{1}{\beta}\ln(\alpha\beta) + \frac{1}{\beta} lnt \quad (5)$$

where α (mg g^{-1} min^{-1}) represents the initial adsorption rate and β (g mg^{-1}) is related to surface heterogeneity. Intraparticle diffusion was evaluated using

$$q_t = k_{id} t^{1/2} + C \quad (6)$$

Where k_{id} (mg g^{-1} $min^{-1/2}$) is the intraparticle diffusion rate constant and C (mg g^{-1}) reflects boundary layer thickness.

Equilibrium data were analysed using Langmuir, Freundlich, Temkin, and Dubinin–Radushkevich (D-R) isotherms. The linearized Langmuir equation is

$$\frac{1}{q_e} = \frac{1}{K_L q_{max}} \cdot \frac{1}{C_e} + \frac{1}{q_{max}} \quad (7)$$

where q_{max} (mg g^{-1}) is the maximum adsorption capacity, K_L (L mg^{-1}) is the Langmuir constant, and Ce (mg L^{-1}) is the equilibrium concentration. The Freundlich model is expressed as

$$\log q_e = \log K_F + \frac{1}{n}\log C_e \quad (8)$$

Where K_F and n are the Freundlich constants related to adsorption capacity and intensity. The Temkin model is given by

$$\ln q_e = \ln a + \frac{RT}{b}\ln C_e \quad (9)$$

where a (L g^{-1}) is the Temkin isotherm constant, b (J mol^{-1}) relates to adsorption heat, R is the

gas constant, and T is temperature (K). The D-R isotherm is expressed as

$$\ln q_e = \ln q_m - K\varepsilon^2 \quad (10)$$

where q_m (mg g^{-1}) is the theoretical saturation capacity, K (mol^2 J^{-2}) is a constant related to adsorption energy, and (ε^2=RT\ln(1+1/Ce).

The mean free energy of adsorption E (kJ mol^{-1}) was calculated using

$$E = \frac{1}{\sqrt{2K}} \quad (11)$$

Model parameters were obtained by linear regression, and the goodness of fit was assessed using the coefficient of determination (R^2).

Thermodynamic Analysis

Thermal effects were studied through 298 to 318 K. Thermodynamic parameters, including Gibbs free energy (ΔG^0), enthalpy (ΔH^0), and entropy (ΔS^0), were derived from the following relations in equation 12 and 13:

$$K_0 = \frac{q_e}{C_e} \quad (12)$$

$$\Delta G^o = -RTlnK_0 \quad (13)$$

$$lnK_0 = \frac{\Delta S^o}{R} - \frac{\Delta H^o}{RT} \quad (14)$$

Where K_o is the thermodynamic equilibrium constant (distribution coefficient), R is the universal gas constant (8.314 J mol^{-1} K^{-1}), and T is the absolute temperature (K). The values of ΔH° and ΔS° were obtained from the slope and intercept, respectively, of the linear Van't Hoff plot of ln K_0 versus 1/T

Supplementary Studies

Reusability Assessment

The reusability of the adsorbents was evaluated through desorption experiments using 0.01 M HCl or 0.01 M NaOH. After desorption, the materials were heated at 55 °C, centrifuged, washed thoroughly, dried, and reused for up to four adsorption cycles. Adsorption performance after each cycle was asses using UV–Visible spectrophotometry at 497 nm (CR) and 460 nm (MO) respectively.

RESULT AND DISCUSSION

Characterization of produced FeNps/MMS

FTIR spectroscopic analysis

FTIR spectroscopy confirmed the successful synthesis of the FeNps/MMS composite and the interactions between the iron nanoparticles and the modified maize stalk. The spectrum of modified maize stalk (MMS) (Figure 1) showed characteristic absorptions, including a broad O–H stretching vibration near 3300 cm^{-1}, a C–O symmetric stretch of carboxylates at 1415 cm^{-1}, a C–O–C stretch at 1215 cm^{-1}, and a C–O stretch in cellulose at 1033 cm^{-1} [22, 23]. The spectrum of the pure FeNps exhibited characteristic Fe–O vibration bands at 1122, 974, 896, and 778 cm^{-1} [25]. The broad O–H band observed at 3376 cm^{-1} in the FeNps spectrum is likely associated with α-FeOOH (goethite), which was also identified as the dominant phase in FeNps in XRD analysis (Figure 3).

The FTIR spectrum of the FeNps/MMS composite retained the major functional group peaks of the MMS, with slight shifts in band positions, such as the C–O stretching band from 1033 to 1038 cm^{-1}, together with the characteristic Fe–O vibration at 778 cm^{-1} [8]. The presence of both MMS and Fe–O bands, together with these small shifts, confirms the successful incorporation of iron nanoparticles onto the modified maize stalk. These changes suggest interactions between the Fe sites on the nanoparticle surface and the oxygen-containing functional groups (–OH and $–COO^-$) of the MMS through coordination bonding. Similar FTIR observations have been reported in previous studies [8].

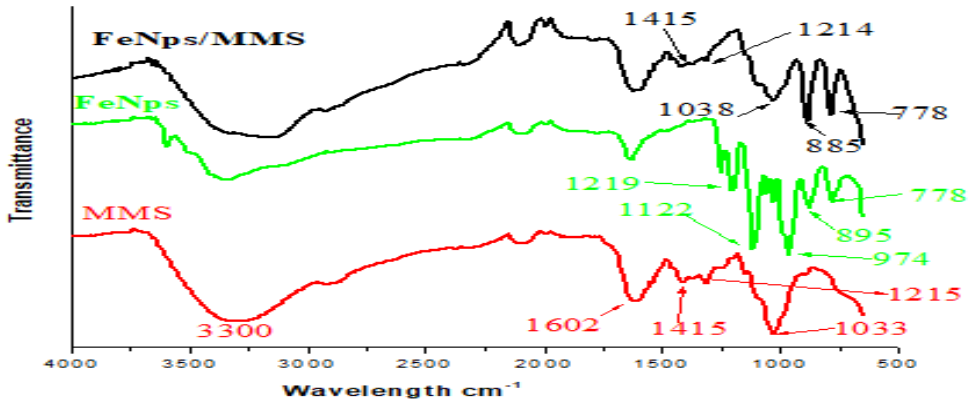

Figure 1: FTIR spectrum of MMS, FeNps and FeNps/MMS

Scanning Electron Microscopy (SEM) analysis

SEM was used to examine the surface morphology of the pure iron nanoparticles (FeNps), modified maize stalk (MMS), and the FeNps/MMS composite. The SEM images are presented in Figure 2.

The SEM image of the FeNps (Fig. 2a) showed that the nanoparticles were highly aggregated, forming large, irregular, block-like clusters, similar to those reported in previous studies [23, 26]. This aggregation is likely due to the high surface energy of the nanoparticles, resulting in a rough surface with spaces between the particles that contribute to porosity [22, 25].

The SEM image of the modified maize stalk (MMS) (Fig. 2b) showed a rough, flaky, and layered surface typical of chemically treated lignocellulosic biomass [5, 13]. The chemical treatment partially removed hemicellulose and lignin, producing a fibrous structure with irregular flakes and interconnected pores. These features increased the surface roughness and porosity of the material, which is consistent with previous studies on modified agricultural biomass [5, 13, 26].

The SEM image of the FeNps/MMS composite (Fig. 2c) confirmed that the FeNps were successfully attached to the surface of the modified maize stalk. The composite showed a rough and porous surface with the layered structure of MMS still visible. Many small bright particles, representing the FeNps, were distributed over the surface.

The nanoparticles appeared as clusters rather than a uniform layer, indicating strong interactions between the FeNps and the functional groups on the MMS [5, 11].

This rough and porous structure agrees with the BET results (Table 1), which showed that the composite has a high surface area and pore volume, making it suitable for efficient adsorption.

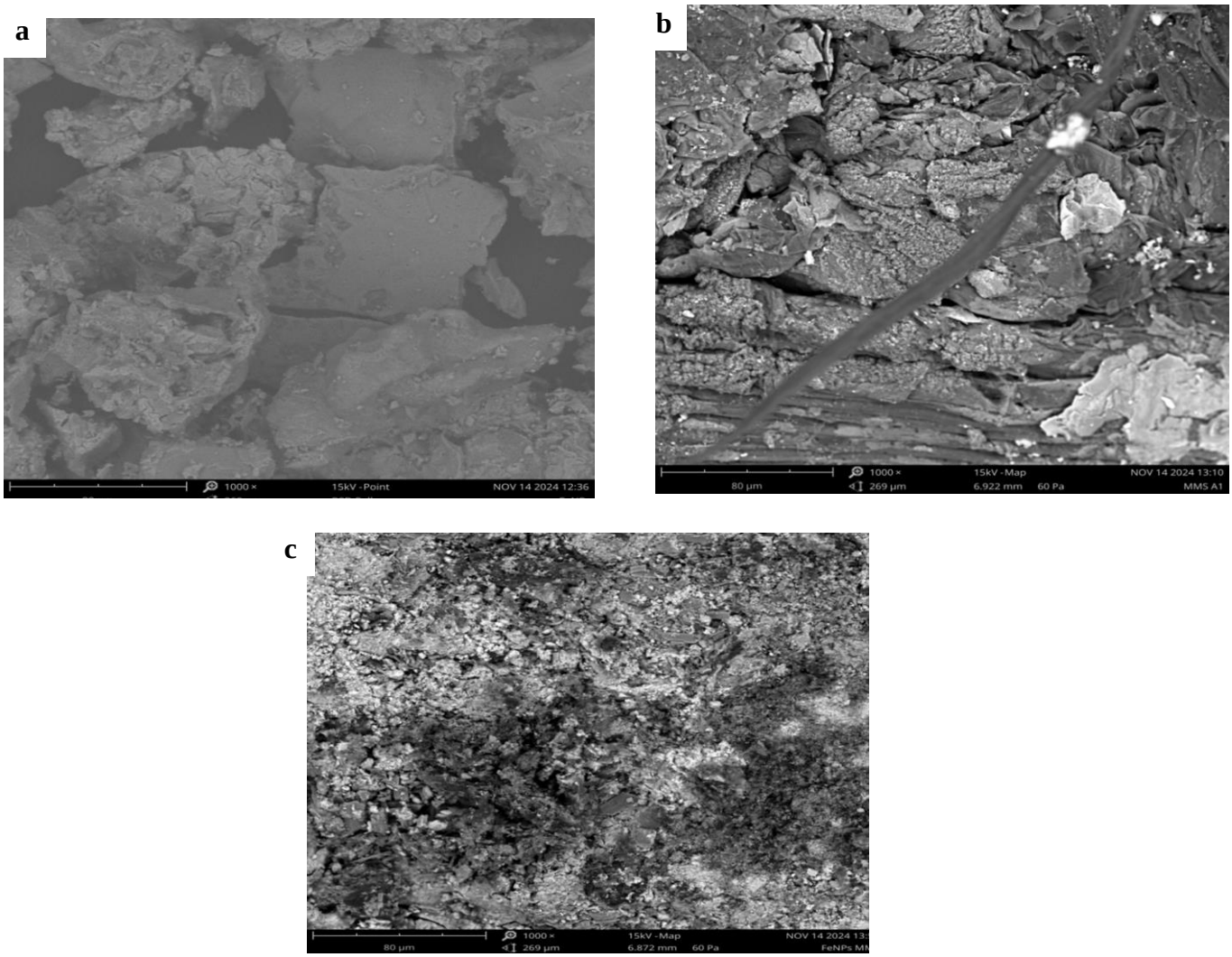

Figure 2: SEM image of a) FeNPs b) MMS, and c). FeNps/MMS composite

X-ray diffraction analysis

The XRD pattern as presented on Figure 3 is dominated by broad and diffuse reflections in the 2θ range of 20–30°, indicating a largely amorphous structure with embedded nanocrystalline domains, a characteristic feature of iron-based nanoparticles synthesised via aqueous routes [28, 29].

Phase identification revealed that goethite (α-FeOOH) is the predominant phase, accounting for approximately 73% of the sample, with minor contributions from hematite (α-Fe_2O_3) and melanterite ($FeSO_4 \cdot 7H_2O$)[30]. Diffraction peaks at 21.085° and 24.028° confirm the presence of oxidised iron species, while a weak reflection at 26.938° corresponds to metallic iron (α-Fe), indicating partial reduction during synthesis[30, 31]. An additional peak at 35.640° suggests the presence of spinel-type iron oxides, such as magnetite or maghemite, which are associated with magnetic properties [28]. The average crystallite size using the highest peak at

26.94^0, estimated via the Derby Scherrer equation (Eqn 15), was approximately 83 nm, confirming the nanoscale dimensions of the primary particles.

$$D = {K\lambda}/{(\beta Cos\theta)} \quad (15)$$

Using the most intense peak at 2θ = 26.938° (corresponding to metallic α-Fe). λ is wavelength of X-ray radiation (1.5418 Å), β (0.25^0) is full-width at half (FWHM) of the intense peak at diffracted angle (2θ value)

The XRD pattern of the FeNps/MMS composite demonstrated a notable evolution in structure. The composite retained an amorphous character, quantitative analysis indicated a shift in the iron oxide phase distribution. The relative proportion of goethite decreased, while the hematite fraction increased, suggesting the modified maize stalk matrix influenced nucleation kinetics and favoured hematite formation during composite synthesis [22, 30–32].

New diffraction peaks emerged in the composite pattern, notably at low (2θ = 8.56°) and high (2θ = 67.97°) angles. These peaks, absent in the pure FeNps, are tentatively assigned to iron oxyhydroxide layered structures and a well-crystallized maghemite phase, respectively [34]. The persistence of characteristic FeNps peaks, alongside changes in their intensity and slight shifts in d-spacing confirms successful composite formation and suggests strong interfacial interactions between the nanoparticles and the functionalized biomass support [22, 30–32]. The average crystallite size for the FeNps/MMS composite was estimated to be approximately 52 nm, representing a significant reduction relative to the FeNps and further confirming the stabilising and size-controlling effect of the modified maize stalks [22, 30–32].

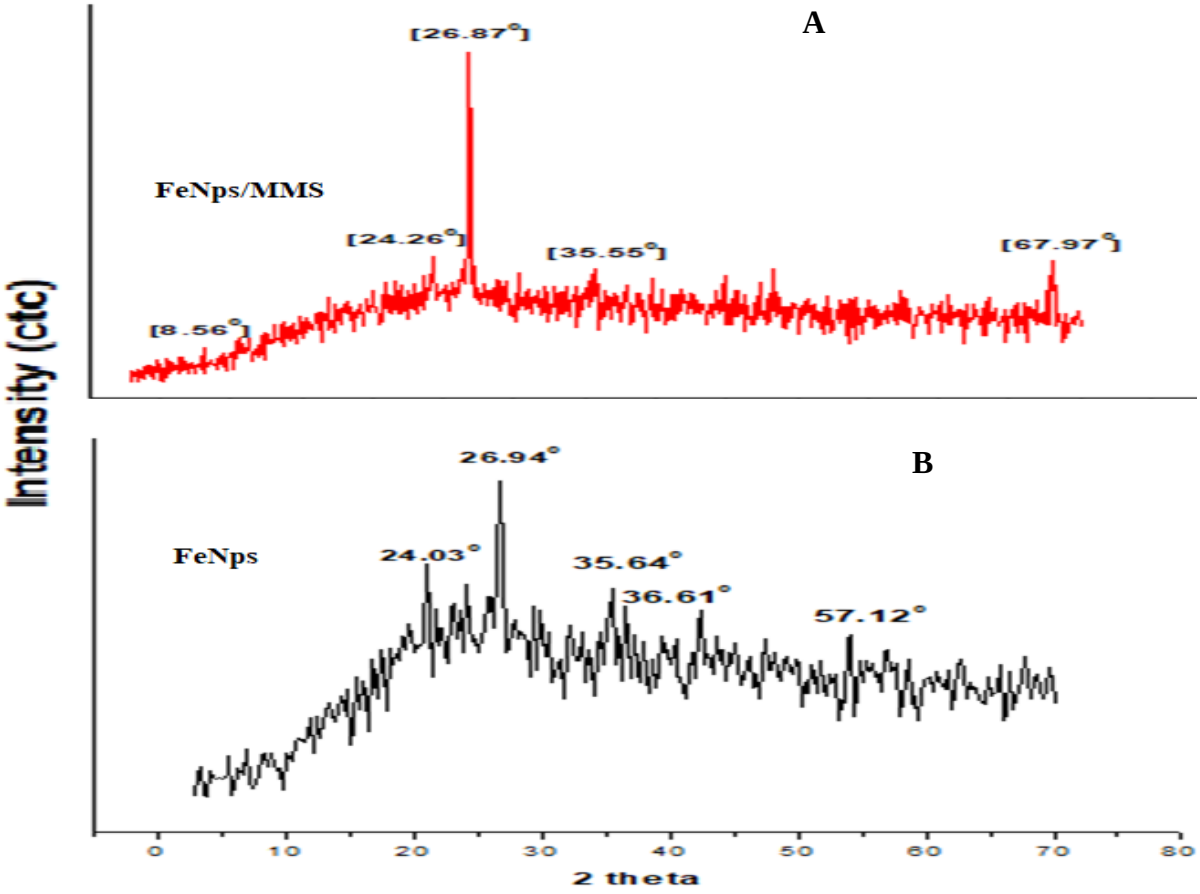

Figure 3: XRD pattern of FeNps (A) and FeNps/MMS (B)

Brunauer-Emmett-Teller (BET) Analysis

Nitrogen physisorption analysis was performed to characterize the specific surface area and pore structure of the synthesized materials and the results presented in Table 1. The iron nanoparticles (FeNps) exhibited a high BET surface area of 139.8 $m^2 g^{-1}$. Pore size distribution analysis (BJH method) indicated a mesoporous structure with an average pore diameter of 2.11 nm and a pore volume of 0.082 $cm^3 g^{-1}$. Dubinin-Astakhov (DA) analysis further revealed a micropore volume of 0.188 $cm^3 g^{-1}$ and a low adsorption energy of 0.800 kJ mol^{-1}, characteristic of a physical adsorption mechanism driven by weak van der Waals interactions[34, 35].

The formation of the FeNps/MMS composite resulted in a substantial enhancement of textural properties. The composite's BET surface area increased significantly to a range of 250–273 $m^2 g^{-1}$. This dramatic increase is attributed to the integration of the high-surface-area, porous modified maize stalk (MMS) matrix, which effectively disperses the FeNps and provides additional structural porosity [37]. Correspondingly, the DA adsorption energy for

the composite rose to 1.715 kJ mol^{-1}, suggesting stronger adsorbate-adsorbent interactions likely due to the presence of functional groups on the MMS support [34, 36]. The average pore diameter was refined to 2.18 nm. The composite's superior surface area, combined with its tailored porosity and increased adsorption energy, demonstrates a synergistic effect that yields an adsorbent architecture with highly accessible active sites, making it promising for enhanced contaminant removal applications [34–36].

Table 1: BET Textural Properties of FeNps and FeNps/MMs

Parameter	FeNps	FeNps/MMs
BET surface area (m^2 g^{-1})	139.773	249.946
BJH surface area (m^2 g^{-1})	167.895	273.384
BJH pore volume (cc g^{-1})	0.082	0.129
BJH pore diameter (nm)	2.108	1.793
DA micropore volume (cc g^{-1})	0.188	0.18
DA mode pore diameter (nm)	2.8	2.18
DA adsorption energy, E (kJ mol^{-1})	0.8	1.715

BATCH ADSORPTION

Effect of FeNps/MMS dosage in the removal Congo Red and Methyl Orange

The FeNps/MMS composite (Figure 4) demonstrated effective adsorption of the synthetic dyes CR and MO. The result indicate dye removal increased progressively with dosage, following the typical trend of enhanced adsorption capacity with a larger number of available binding sites [37, 38]

At 120 mg dosage, the composite achieved removal efficiencies of 81% for Congo red and 78% for Methyl Orange. These values indicate strong interactions between the dye molecules and the FeNps/MMS support [5]. The relatively higher dye removal can be explained by multiple interaction mechanisms, including hydrogen bonding and π–π stacking between the aromatic structures of the dyes and the lignocellulosic components of MMS [5, 39]. These interactions provide multiple binding modes beyond simple electrostatic attraction [5, 39].

The steadily increasing removal efficiency across the dosage range suggests that the composite maintains an accessible and well-dispersed surface structure even at higher masses, allowing effective interaction between dye molecules and the available active sites [4, 5, 39].

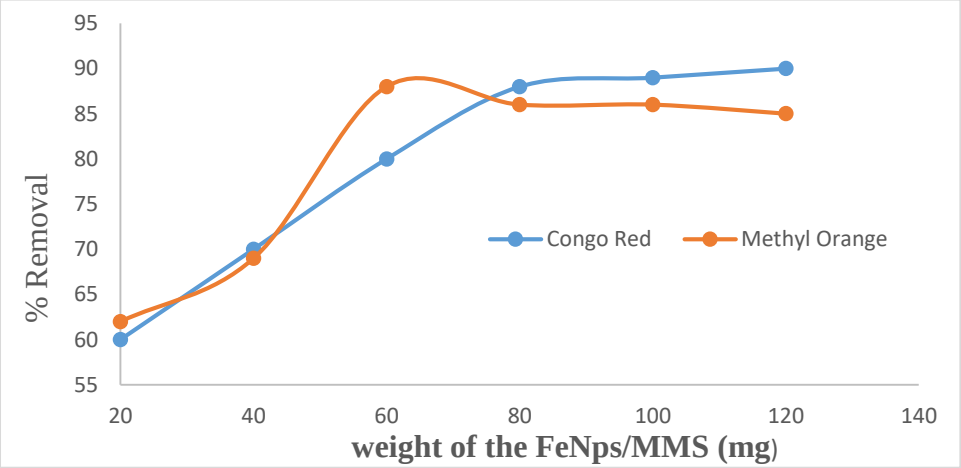

Figure 4: The effect of FeNps/MMS dosage on the removal of CR and MO

Effect of contact time on the removal Congo Red and Methyl Orange

CR and MO showed rapid adsorption onto FeNps/MMS during the first 5–10 minutes (Figure 5). This rapid uptake corresponds to the strong interaction of dye molecules with the porous biomass matrix and the surface of the supported FeNps [5, 39]. CR adsorption reached near-equilibrium (~81% removal) within 25-30 minutes while MO adsorption exhibited a distinct pattern, characterized by a slower initial uptake that accelerated after 10 minutes, reaching a plateau of approximately 70% removal after 20 minutes. This kinetic behaviour for MO may indicate an initial period of molecular reorientation or pore entry prior to effective binding due molecular size or steric factor[5, 39]. Equilibrium for both dyes was established within the 35-minute experimental timeframe

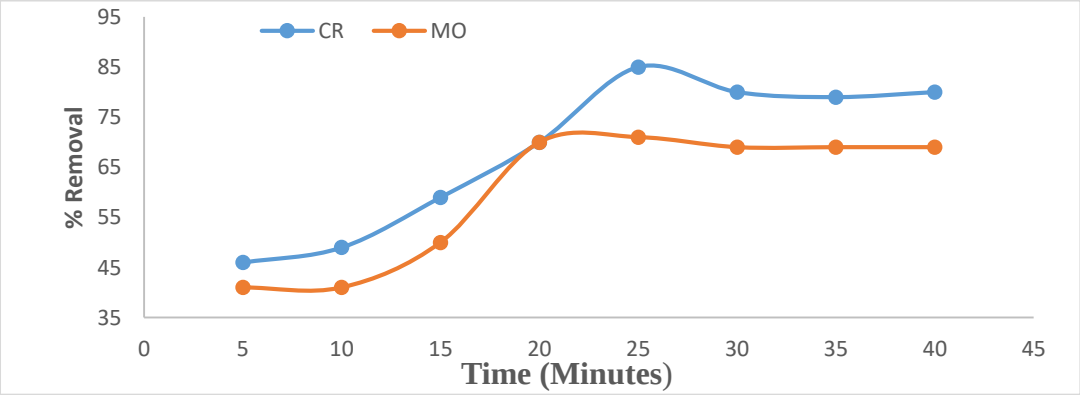

Figure 5: Effect of contact time on the removal CR and MO on FeNps/MMS

Effect of pH on the Removal Congo Red and Methyl Orange

The adsorption efficiency of Congo red by the FeNps/MMS composite exhibited a pronounced dependence on solution pH, with maximal removal observed under acidic conditions (pH 3–5) (Figure 6). This behaviour is attributed to the protonation of surface functional groups (e.g., -OH, -COOH) on the composite at low pH, generating a positively charged surface that facilitates strong electrostatic attraction with the anionic sulfonate groups ($-SO_3^-$) of the CR dye [42]. As the pH increased, progressive deprotonation of the adsorbent surface occurred, leading to a reduction in positive charge density and a consequent decrease in electrostatic interaction forces [5, 42]. This resulted in a steady decline in dye uptake, a trend consistent with the typical adsorption behaviour of anionic azo dyes onto metal oxide–biochar composites, where electrostatic attraction is a primary removal mechanism [5, 41, 42]

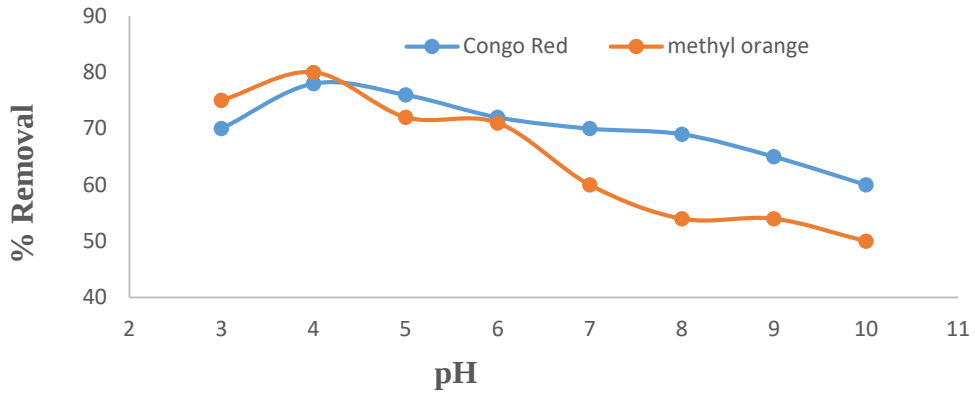

Figure 6: Effect of pH on the Removal CR and MO on FeNps/MMS

A similar pH-dependent adsorption profile was observed for MO (Figure 6), which also demonstrated optimum removal at low pH. The high adsorption capacity under acidic conditions is driven by the favourable electrostatic interaction between the protonated, positively charged surface of the FeNps/MMS composite and the anionic chromophores of the dye molecule [44]. With increasing pH, deprotonation diminishes the availability of these charged binding sites, thereby reducing the adsorption capacity. This correlation between surface charge and dye uptake aligns with established reports on the pH-sensitive adsorption of anionic dyes, confirming the critical role of electrostatic interactions in the adsorption process [40]

Kinetic a Study of Congo Red and Methyl Orange on FeNps/MMS

To elucidate the adsorption mechanism and identify the rate-controlling steps, the kinetic data for Congo red and methyl orange were fitted to the pseudo-first-order (PFO), pseudo-second-

order (PSO), Elovich, and intraparticle diffusion models, with the resulting parameters presented in Table 2. The PFO model, which assumes that the adsorption rate is proportional to the number of unoccupied active sites [45] exhibited only moderate agreement with the experimental data. The correlation coefficients obtained for CR (R^2 = 0.9144) and MO (R^2 = 0.9266) suggest that dye adsorption may partially follow first-order kinetics [46]. However, the calculated equilibrium adsorption capacities were significantly lower than the experimentally determined values. The PFO model predicted q_e,cal values of 4.35 mg g^{-1} for CR and 5.03 mg g^{-1} for MO, compared with the corresponding experimental capacities (q_e,exp) of 7.23 and 7.13 mg g^{-1}, respectively. Such discrepancies indicate that the PFO model does not adequately represent the adsorption behaviour of the investigated dyes. Similar observations were reported by Shrestha et al. [15], who found that unrealistic q_e values obtained from the PFO model reflected adsorption mechanisms extending beyond simple physical attraction.

In contrast, the PSO model provided the best description of the adsorption process. Excellent linearity was obtained, with R^2 values exceeding 0.95 and reaching 0.9791 for CR. moreover, the calculated equilibrium adsorption capacities closely matched the experimental values. For CR, q_e,cal and q_e,exp were 7.18 and 7.23 mg g^{-1}, respectively, while for MO the corresponding values were 7.46 and 7.13 mg g^{-1}. The close agreement between experimental and predicted capacities confirms that the PSO model accurately describes the adsorption kinetics of both dyes [46, 47]. Since the PSO model is commonly associated with chemisorption involving electron sharing or exchange between adsorbate and adsorbent [49], the results suggest that surface chemical interactions play a dominant role during dye uptake.

The kinetic parameters further support this interpretation. The PSO rate constant (k_2) was highest for CR (0.01480 g mg^{-1} min^{-1}), indicating faster adsorption kinetics compared with MO. Similarly, the initial adsorption rate (h) followed the order CR (0.764 mg g^{-1} min^{-1}) > MO (0.619 mg g^{-1} min^{-1}). The superior adsorption rate observed for CR can be attributed to its aromatic structure and multiple sulfonate groups, which promote strong electrostatic interactions, hydrogen bonding, and π–π interactions with the functional groups present on the adsorbent surface. Similar observations have been reported for biomass-supported nanomaterials and composite adsorbents by [5, 49, 50].

The Elovich model, which is frequently applied to chemisorption processes occurring on heterogeneous surfaces [45], also showed reasonable agreement with the experimental data. The model produced correlation coefficients ranging from 0.8503 to 0.9307, with MO exhibiting the highest R^2 value. The initial adsorption rate parameter (α) varied considerably

between the dyes, with CR showing a substantially higher value (7.74 mg g^{-1} min^{-1}) than MO (2.96 mg g^{-1} min^{-1}). This result indicates that CR molecules interact more rapidly with the adsorbent surface, likely due to the presence of multiple functional groups capable of forming strong intermolecular interactions [47, 51]. The desorption constant (β) was also highest for CR (1.015 g mg^{-1}), suggesting stronger binding affinity and lower desorption tendency. Comparable findings were reported by Juturu et al (2020) [52], who observed rapid CR adsorption on iron-based nanocomposites. Nevertheless, the lower R^2 values obtained from the Elovich model relative to the PSO model indicate that surface heterogeneity alone cannot fully explain the adsorption process [44, 51].

The contribution of diffusion mechanisms was assessed using the Weber-Morris intraparticle diffusion model. Strong linearity was observed for both dyes, particularly for CR (R^2 = 0.9727), indicating the involvement of pore diffusion during adsorption. However, the regression lines did not pass through the origin, as reflected by the non-zero intercept values, confirming that intraparticle diffusion was not the sole rate-limiting step [3, 50]. The intercept values suggest the simultaneous influence of external mass-transfer resistance and boundary-layer diffusion. Similar observations have been reported by for adsorption systems involving composite adsorbents [44, 47].

To further clarify the diffusion mechanism, a three-stage intraparticle diffusion analysis was performed attached in appendix. The first stage corresponded to rapid external film diffusion, the second stage represented gradual intraparticle diffusion, while the third stage reflected equilibrium attainment. The first two stages exhibited excellent linearity (R^2 = 0.9167–0.9931), whereas the third stage displayed negligible slopes and adsorption capacities that closely matched the experimentally observed equilibrium values. Notably, the intraparticle diffusion rate during the second stage was greater than the first-stage diffusion rate for CR (0.7426 vs. 0.3598), indicating that once the boundary-layer resistance was overcome, dye molecules diffused efficiently into the internal pore structure of the adsorbent [37]. These findings demonstrate that dye adsorption proceeds through multiple transport steps but is ultimately governed by surface-controlled interactions, as evidenced by the superior performance of the PSO model. Similar conclusions were reported by [44, 47].

Table 2: Kinetic study of CR and MO on FeNps/MMS paramaters

Kinetic Model	Parameter	CR	MO
Pseudo-First-Order	R^2	0.9144	0.9266
	k_1 (min^{-1})	0.025	0.0292
	q_e,exp (mg/g)	7.23	7.13
	q_e,cal (mg/g)	4.35	5.03
Pseudo-Second-Order	R^2	0.9791	0.974
	k_2 (g/mg·min)	0.0148	0.0111
	q_e,exp (mg/g)	7.23	7.13
	q_e,cal (mg/g)	7.18	7.46
	h (mg/g·min)	0.764	0.619
Elovich	R^2	0.9101	0.9307
	α (mg/g·min)	7.74	2.96
	β (g/mg)	1.015	0.803
Intraparticle Diffusion	R^2	0.9727	0.9672
	k_id (mg/g·$min^{1/2}$)	0.4406	0.4788
	C (mg/g)	2.8	2.41

Isotherm Study of Congo Red and Methyl Orange on FeNps/MMS.

The adsorption behaviour of Congo Red and Methyl Orange on the FeNps/MMS composite was evaluated using equilibrium isotherm models to elucidate the nature of dye surface interactions and result presented in Table 3. The Langmuir model provided moderate correlations for both dyes (R^2 = 0.8372 for CR and 0.8898 for MO), with estimated maximum monolayer capacities (q_{max}) of 7.62 mg g^{-1} and 51.81 mg g^{-1}, respectively. The substantially higher q_{max} obtained for MO can be attributed to its smaller molecular size and simpler molecular structure, which favour more efficient packing and accessibility to active sites on the adsorbent surface [4, 34, 43]. The corresponding Langmuir constants (K_L) of 0.0251 L mg^{-1} for CR and 0.00889 L mg^{-1} for MO indicate moderate binding affinity between the dyes and the FeNps/MMS surface [4, 43].

In contrast, the Freundlich isotherm exhibited an excellent fit to the experimental data, with correlation coefficients of 0.9953 for CR and 0.9588 for MO, suggesting that adsorption predominantly occurs on a heterogeneous surface through multilayer formation[34, 52]. The Freundlich capacity constants (K_F) of 0.280 for CR and 0.584 for MO further support the higher

uptake tendency for MO [51]. Moreover, the Freundlich intensity parameters (n = 1.244 for CR and 1.161 for MO) exceeded unity, confirming that the adsorption of both dyes is favourable and occurs under energetically favourable conditions [3, 4, 43, 50].

The Temkin heat of adsorption (b_T) was calculated as 998 J mol^{-1} for CR and 407 J mol^{-1} for MO, indicating relatively stronger dye surface interactions for CR. This behaviour may be associated with π-π interactions between the extended aromatic structure of CR and surface functional groups of the FeNps/MMS composite, whereas MO adsorption is likely governed primarily by electrostatic attractions [3, 4, 34, 43, 50].

The Dubinin-Radushkevich (D–R) isotherm further clarified the adsorption mechanism, yielding mean adsorption energies (E) of 5.16 kJ mol^{-1} for CR and 5.79 kJ mol^{-1} for MO. These values fall within the characteristic range of physisorption (E < 8 kJ mol^{-1}), indicating that weak physical forces such as van der Waals interactions and electrostatic attraction dominate the adsorption process [3, 4, 43, 50]. The combined isotherm analyses demonstrate that CR and MO adsorption onto FeNps/MMS proceeds as a favourable, multilayer process on a heterogeneous surface, predominantly controlled by physisorptive mechanisms.

Thermodynamic Study of the Adsorption Behaviour of Congo Red and Methyl Orange on FeNps/MMS

Thermodynamic analysis provides critical insight into the spontaneity and binding mechanisms of Congo Red and Methyl Orange adsorption onto the FeNps/MMS composite (Table 4). The adsorption of CR was found to be endothermic (ΔH° = +3.17 kJ mol^{-1}), with a positive entropy change (ΔS° = +19.08 J mol^{-1} K^{-1}) and negative Gibbs free energy (ΔG° < 0) across all temperatures studied. This thermodynamic profile indicates an entropy-driven process [32, 34, 53]. The positive ΔS° suggests a significant increase in randomness at the solid-liquid interface, predominantly due to the displacement of ordered water molecules surrounding the hydrophobic, aromatic structure of CR upon adsorption [32, 34, 53]. This mechanism is consistent with the behaviour of large, planar dyes interacting with heterogeneous iron-based surfaces, where dehydration and solvent reorganization provide the primary thermodynamic driving force [32, 34, 44, 53].

In contrast, MO adsorption exhibited a strongly exothermic (ΔH° = –15.49 kJ mol^{-1}) and highly spontaneous process, with a large positive entropy change (ΔS° = +43.95 J mol^{-1} K^{-1}) and substantially negative ΔG° values (–29 kJ mol^{-1}).

Table 3: Isotherm study of CR and MO on FeNps/MMS Parameters

Model	Parameter	CR	MO
Langmuir	R^2	0.8299	0.8898
	q_{max} (mg/g)	7.62	51.81
	K_L ($L \cdot mg^{-1}$)	0.02506	0.008887
	R_L	0.47	0.714
Freundlich	R^2	0.9588	0.9953
	K_F [$(mg/g)(L/mg)^{1/n}$]	0.2803	0.5837
	N	1.2438	1.1609
Temkin	R^2	0.9699	0.9711
	b_T (J/mol)	998.42	407.39
	K_T (L/mol)	0.1964	0.1975
D–R	R^2	0.92	0.8833
	qDR (mg/g)	4.89	10.98
	β (mol^2/kJ^2)	1.88×10^{-2}	1.49×10^{-2}
	E (kJ/mol^1)	5.16	5.79

This combination of a favourable enthalpy change and a significant entropy gain points to a synergistic adsorption mechanism [12, 34, 39]. The exothermicity suggests strong, specific interactions such as electrostatic attraction or surface complexation between the sulfonate groups of MO and the composite's active sites [12, 34, 39]. Concurrently, the large positive ΔS° indicates extensive desolvation and increased interfacial disorder, likely from the release of water molecules from both the adsorbent surface and the hydrated dye [12, 34, 39]. Similar mixed enthalpy-entropy driven processes have been documented for MO adsorption on various metal-based nanomaterials [39, 40].

The distinct thermodynamic pathways for CR and MO highlight the influence of molecular structure on adsorption energetics. The more aromatic, bulkier CR molecule favours an entropy-driven process dominated by hydrophobic and π-π interactions, while the smaller, more polar MO molecule engages in stronger, specific exothermic interactions with the

adsorbent surface, enhanced by significant concomitant desolvation [39, 40, 54]. These differences underscore the composite's versatile binding capability and provide a thermodynamic rationale for its effectiveness in treating wastewater containing multiple dye structures.

Table 4: Thermodynamic study parameters of CR and MO adsorption study on FeNps/MMS

Adsorbate	Temperature (K)	ΔG^0 (J/mol)	ΔH^0 (J/mol)	ΔS^0 (J/mol)	R^2
CR	298	-3759.3	3165.97	23.24	0.9516
	303	-3875.5			
	308	-3991.7			
	313	-4107.9			
	318	-4224.1			
MO	298	-28583	-15486	43.95	0.9144
	303	-28803			
	308	-29022			
	313	-29242			
	318	-29462			

Reusability Study for FeNps/MMS Composite.

The FeNps/MMS composite demonstrated excellent stability and reusability for the removal of Congo Red and Methyl Orange (Figure 7). The composite retained a high and stable adsorption capacity across all four cycles. CR removal remained consistently high, decreasing only marginally from 90% in the first cycle to 83% in the fourth. MO adsorption showed remarkable stability, with removal efficiency maintaining 86% in the first cycle and 85% in the fourth. This sustained performance indicates that the binding of these anionic dyes to the composite is dominated by reversible physisorptive mechanisms. Interactions such as π-π stacking, hydrogen bonding, and electrostatic attraction can be effectively disrupted during the desorption step without causing permanent damage or blockage to the adsorbent's active sites, allowing for efficient regeneration and reuse[55].

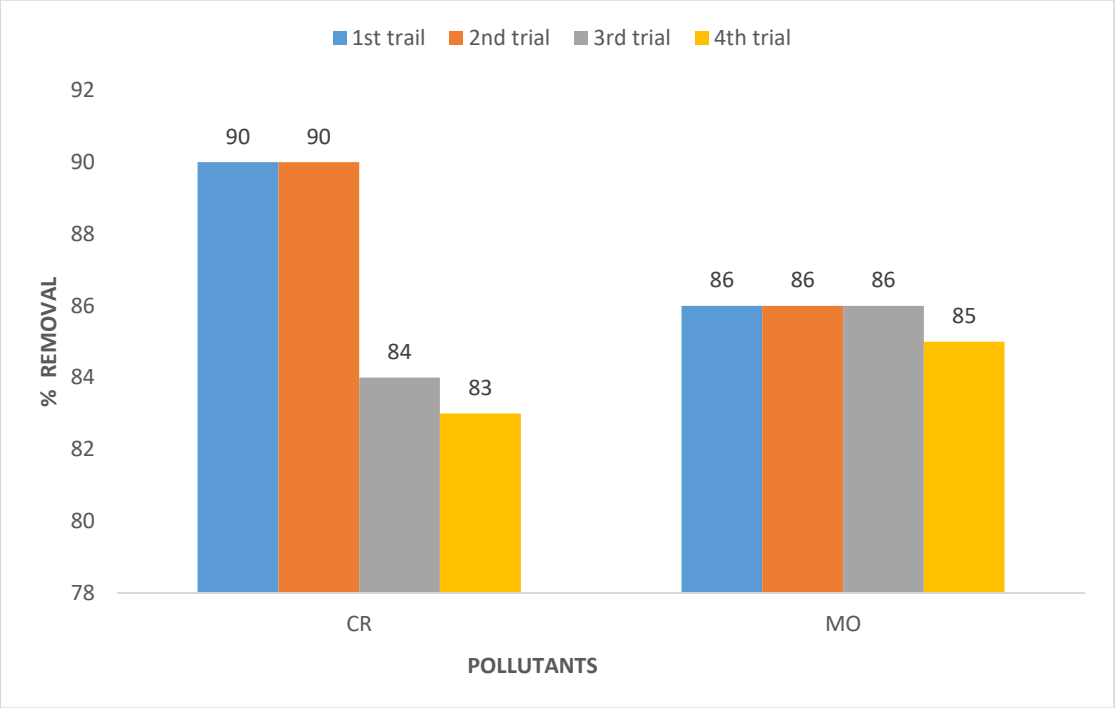

Figure 7: Reusability Study for FeNps/MMS Composite

Conclusion

This study successfully synthesized an iron nanoparticle/modified maize stalk (FeNps/MMS) composite through a microwave-assisted co-precipitation method using maize stalk as a low-cost and sustainable support material. Characterisation by FTIR, SEM, XRD, and BET confirmed the successful formation of the composite, with an average crystallite size of 51.92 nm, a high specific surface area of 249.94 $m^2\ g^{-1}$**,** and a well-developed micro-mesoporous structure that enhanced its adsorption performance.

The FeNps/MMS composite effectively removed Congo Red and Methyl Orange from aqueous solutions, achieving maximum removal efficiencies of 90% and 86%, respectively. The adsorption process followed the pseudo-second-order kinetic model ($R^2 \geq 0.974$) with experimental adsorption capacities of 7.23 mg g^{-1} for CR and 7.13 mg g^{-1} for MO. Isotherm data were best described by the Freundlich isotherm ($R^2 = 0.9588$ for CR and 0.9953 for MO), indicating multilayer adsorption on a heterogeneous surface. Dubinin–Radushkevich adsorption energies of 5.16 kJ mol^{-1} (CR) and 5.79 kJ mol^{-1} (MO) showed that physisorption was the dominant adsorption mechanism. Thermodynamic analysis further revealed that CR adsorption was spontaneous and endothermic, whereas MO adsorption was spontaneous and exothermic.

The composite also showed excellent stability, maintaining 83% and 85% removal efficiencies for CR and MO, respectively, after four adsorption–desorption cycles. These findings demonstrate that FeNps/MMS is an efficient, reusable, low-cost, and environmentally friendly adsorbent with strong potential for the treatment of dye-contaminated wastewater and future large-scale environmental remediation.

References

[1] Abdelbasir, S. M., Mccourt, K. M., Lee, C. M. & Vanegas, D. C. (2020). Waste-Derived Nanoparticles: Synthesis Approaches , Environmental Applications , and Sustainability Considerations. *Frontiers in Chemistry*, *8*(August), 1–18. https://doi.org/10.3389/fchem.2020.00782

[2] Rashid, R., Shafiq, I., Akhter, P., Iqbal, M. J. & Hussain, M. (2021). A state-of-the-art review on wastewater treatment techniques: the effectiveness of adsorption method. *Springer Nature Journal*, *2*(2170), 1–20. https://doi.org/10.1007/s11356-021-12395-x

[3] Garg, S., Singh, S., Khan, N. A., Samuel, J., Ramamurthy, P. C. & Singh, J. (2024). Equilibrium and kinetic modeling of Cr (VI) removal by novel tolerant bacteria species along with zero - valent iron nanoparticles. *Scientific Reports*, *14*(8611), 1–12. https://doi.org/10.1038/s41598-024-57835-z

[4] Majadleh, M., Shahwan, T., Ahmed, R. B. & Anjass, M. (2022). Application of Fe and Cu nanoparticles for methyl orange removal from water and water-ethanol mixtures under various experimental conditions. *Water Resources and Industry*, *28*(September), 100189. https://doi.org/10.1016/j.wri.2022.100189

[5] Yadav, V. K., Gnanamoorthy, G., Ali, D., Bera, S. P., Roy, A., Kumar, G., Choudhary, N., Kalasariya, H. & Basnet, A. (2022). Cytotoxicity, Removal of Congo Red Dye in Aqueous Solution Using Synthesized Amorphous Iron Oxide Nanoparticles from Incense Sticks Ash Waste. *Journal of Nanomaterials*, *2022*. https://doi.org/10.1155/2022/5949595

[6] Lam, V. T., Dao, T., Nguyen, H. T., Nguyen, D. T. C., Le, H. & Nguyen, T. D. (2020). Process optimization studies of Congo red dye adsorption onto magnesium aluminium layered double hydroxide using response surface methodology. *Polish. J. Environ. Studies.*, *30*(1), 679–687. https://doi.org/http://doi.10.15244/pjoes/121048

[7] Harja, M., Buema, G. & Bucur, D. (2022). Recent advances in removal of Congo Red dye by adsorption using an industrial waste. *Scientific Reports*, *12*(6087), 1–18. https://doi.org/10.1038/s41598-022-10093-3

[8] Muhammad, N. & Maje, Y. S. (2022). Application of Iron Nanoparticle Coupled with Modified Orange Peel (FeNps/MOP) in Removal of Nickel from Water. *Chemistry Research Journal*, *7*(1), 26–33.

[9] Kumar, R. & Rauwel, P. (2021). Nanoadsorbants for the Removal of Heavy Metals from Contaminated Water : Current Scenario and Future Directions. *Processes*, *9*(1379), 1–29. https://doi.org/doi.org/10.3390/pr9081379

[10] Khedr, M. A., Waly, A. I., Hafez, A. I. & Ali, H. (2012). Synthesis of Modified Chitosan-Montmorillonite Nanocomposite. *Australian Journal of Basic and Applied Sciences*, *6*(6), 216–226.

[11] Rónavári, A., Balázs, M., Szilágyi, Á., Molnár, C., Kotormán, M. & Ilisz, I. (2023). Multi-round recycling of green waste for the production of iron nanoparticles: synthesis, characterization, and prospects in remediation. *Discover Nano*, *18*(8), 1–14. https://doi.org/10.1186/s11671-023-03784-x

[12] Kakavandi, B., Jafari, A. J., Kalantary, R. R., Nasseri, S., Ameri, A. & Esrafily, A. (2013). Synthesis and properties of Fe_3O_4 -activated carbon magnetic nanoparticles for removal of aniline from aqueous solution : equilibrium , kinetic and thermodynamic studies. *Iranian Journal of Environmental Health Sciences & Engineering*, *10*(1), 1. https://doi.org/10.1186/1735-2746-10-19

[13] Shitu, A., Tadda, M. & Abubakar, N. (2014). Utilization of various Agricultural waste materials in the treatment of Industrial wastewater containing Heavy metals : A Review. *International Research Journal of Environment Sciences*, *3*(3), 62–71.

[14] Sadeek, S. A., Negm, N. A., Hefni, H. H. H. & Abdel Wahab, M. M. (2015). Metal adsorption by agricultural biosorbents: Adsorption isotherm, kinetic and biosorbents chemical structures. *International Journal of Biological Macromolecules*, *81*, 400–409. https://doi.org/10.1016/j.ijbiomac.2015.08.031

[15] Shrestha, P., Jha, Kumar, M., Ghimire, Jeevan, Koirala & Raj, A. (2020). Decoration of Zinc Oxide Nanorods into the Surface of Activated Carbon Obtained from Agricultural Waste for Effective Removal of Methylene Blue Dye. *Materials Letters*, *13*(5667), 1–11. https://doi.org/doi:10.3390/ma13245667

[16] Karim, N., Nabil, A., Nogami, M. & Ismail, I. (2020). Preparation of Composite Monolith Supercapacitor Electrode made from Textile-Grade Polyacrylnitrile fibres and Phenolic Resign. *Materials*, *13*(655), 1–125. https://doi.org/10.3390/ma13030655.

[17] Yao, G., Zhu, X., Wang, M., Zhang, Z., Qiu, T. & Qiu, F. (2021). Controlled Fabrication of the Biomass Cellulose–CeO_2 Nanocomposite Membrane as Efficient and Recyclable Adsorbents for Fluoride Removal. *Ind. Eng. Chem. Res.*, *60*(16), 5914–5923. https://doi.org/https://doi.org/10.1021/acs.iecr.1c00012

[18] Liu, X., Yang, L., Zhao, H. & Wang, W. (2020). Pyrolytic production of zerovalent iron nanoparticles supported on rice husk-derived biochar: simple, in situ synthesis and use for remediation of Cr(VI)-polluted soils. *Science of The Total Environment*, *708*, 134479. https://doi.org/https://doi.org/10.1016/j.scitotenv.2019.134479

[19] Al-Radadi, N. S. (2022). Microwave assisted green synthesis of Fe@Au core–shell NPs magnetic to enhance olive oil efficiency on eradication of helicobacter pylori (life preserver). *Arabian Journal of Chemistry*, *15*(5), 103685. https://doi.org/10.1016/J.ARABJC.2022.103685

[20] Yang, X., Tong, J., Yang, X., Shao, X., Luo, T., Zhao, S., Zhang, E., Jiang, B., Wang, L., Han, Y., Zeng, F., Zimmerman, A. R. & Gao, B. (2026). Efficient removal of anionic Congo red by hickory-chip/peanut-shell biochar and Mg-Al hydrotalcite composites fabricated via modified co-precipitation-hydrothermal and buried carbon pyrolysis approach. *Materials Research Bulletin*, *198*, 113963. https://doi.org/https://doi.org/10.1016/j.materresbull.2025.113963

[21] Aivazoglou, E., Metaxa, E. & Hristoforou, E. (2018). Microwave-assisted synthesis of iron oxide nanoparticles in biocompatible organic environment. *AIP Advances*, *8*(4). https://doi.org/10.1063/1.4994057

[22] Fatmahan, O., Karaagac, O. & Hakan, K. (2015). Growth of iron Oxide Nanoparticles by hydrothermal process: effect of reaction parameters on the nanopartcle size. *Journal of Superconductivity and Novel Magnetism*, *28*, 823–829. https://doi.org/DOI 10.1007/s10948-014-2707-9

[23] Mezher, T. A., Ali, A. M. & Abd, A. N. (2023). Iron Oxide Nanoparticle Biosynthesis, Characterization, and Antimicrobial Activity Using Nigella sativa Seeds Extract. *International Journal of Nanoscience*, *22*(4), 1–6. https://doi.org/10.1142/S0219581X23500266

[24] Nadia, N., Suliza, M., Te, L., Alipal, J., Omar, S., Hamidon, N., Hazren, N., Hamid, A., Mohamed, N., Ali, R. & Harun, H. (2020). Evolution of adsorption process for manganese removal in water via agricultural waste adsorbents. *Heliyon*, *6*(September), e05049. https://doi.org/10.1016/j.heliyon.2020.e05049.

[25] Devi, V., Selvaraj, M., Selvam, P., Kumar, A. A., Sankar, S. & Dinakaran, K. (2017). Preparation and Characterization of CNSR functionalized Fe3O4 magnetic nanoparticles: an efficient adsorbent for the removal of Cadmium ion from water. *Biochemical Pharmacology*. https://doi.org/10.1016/j.jece.2017.08.036

[26] Zhang, N., Reguyal, F. & Sarmah, A. K. (2024). Effect of iron nanoparticles on chromium adsorption in aqueous solution using magnetic biochar : A site energy distribution analysis. *Environmental Pollution*, *346*(December 2023), 123593. https://doi.org/10.1016/j.envpol.2024.123593

[27] Hoang, N., Nguyen, V., Nguyen, N., Nguyen, T., Nguyen, T., Hoang Long, N., Huynh, N., Thanh Nhut, T., Ho, N., Nguyen, T. T. & Lê Viết, H. (2022). Preparation, characterization and CDI application of KOH-activated porous waste-corn-stalk-based carbon aerogel. *Journal of Porous Materials*, *30*(4), 1–12. https://doi.org/10.1007/s10934-022-01411-1

[28] Ai, Y., Liu, L., Zhang, C., Qi, L., He, M., Liang, Z., Sun, H. Bin, Luo, G. & Liang, Q. (2018). Amorphous Flowerlike Goethite FeOOH Hierarchical Supraparticles: Superior Capability for Catalytic Hydrogenation of Nitroaromatics in Water. *ACS Applied Materials and Interfaces*, *10*(38), 32180–32191. https://doi.org/10.1021/acsami.8b10711

[29] Harish, V., Ansari, M. M., Tewari, D., Gaur, M., Yadav, A. B., García-Betancourt, M.-L., Abdel-Haleem, F. M., Bechelany, M. & Barhoum, A. (2022). Nanoparticle and Nanostructure Synthesis and Controlled Growth Methods. *Nanomaterials (Basel)*, *12*(18), 3226. https://doi.org/doi: 10.3390/nano12183226

[30] Godymchuk, A., Papina, I., Karepina, E., Kuznetsov, D., Lapin, I. & Svetlichnyi, V. (2019). Agglomeration of iron oxide nanoparticles : pH effect is stronger than amino acid acidity.*Journal of Nanoparticle Research*, *21*(208). https://doi.org/https://doi.org/10.1007/s11051-019-4634-y

[31] Phu, N. D., Ngo, D. T., Hoang, L. H., Luong, N. H., Chau, N. & Hai, N. H. (2011). Crystallization process and magnetic properties of amorphous iron oxide nanoparticles. *Journal of Physics D: Applied Physics*, *44*(34). https://doi.org/10.1088/0022-3727/44/34/345002

[32] Xiaojing, Q., Junhau, Y., Jifeng, Z., Keqiang, Q., Cui, X., Jia, T. & Boliang, L. (2023). A Review of Fe-Based Amorphous and Nanocrystalline Alloys: Preparations, Applications, and Effects of Alloying Elements. *Physica Status Solidi*, *220*(14), 1–15. https://doi.org/http://doi.org/10.1002/pssa.202300079.

[33] Kumar, H., Sinha, S. K., V.Vaibhav, G. & Das, S. (2019). Removal of Cr(VI) by magnetic iron oxide nanoparticles synthesized from extracellular polymeric substances of chromium resistant acid-tolerant bacterium Lysinibacillus sphaericus RTA-01. *Journal of Environmental Health Science and Engineering*, *17*(2), 1001–1016. https://doi.org/10.1007/s40201-019-00415-5

[34] Sewu, D. D., Tran, H. N., Ohemeng-Boahen, G. & Woo, S. H. (2020). Facile magnetic biochar production route with new goethite nanoparticle precursor. *Science of The Total Environment*, *717*, 137091. https://doi.org/10.1016/J.SCITOTENV.2020.137091

[35] Chegeni, A., Babaeipour, V., Fathollahi, M. & Hosseini, S. G. (2022). Modeling of CO2 Adsorption Isotherms, Kinetics and Thermodynamics Equilibrium, and the Brunauer−Emmett−Teller Analysis onto KO_2 Pellets. *Journal of Cluster Science*, *33*(5), 2167–2178. https://doi.org/10.1007/s10876-021-02142-0

[36] Ekwumemgbo, P. A., Shallangwa, G. A., Okon, I. E. & Awodi, I. (2023). Green Synthesis and Characterization of Iron Oxide Nanoparticles using Prosopis Africana Leaf Extract. *Communication in Physical Sciences*, *2023*(2), 125–136.

[37] Zheng, H., Sun, Q., Li, Y. & Du, Q. (2020). Biosorbents prepared from pomelo peel by hydrothermal technique and its adsorption properties for congo red. *Materials Research Express*, *7*(4). https://doi.org/10.1088/2053-1591/AB8A83

[38] Foo, K. Y. & Hameed, B. H. (2010). Insights into the modeling of adsorption isotherm systems. *Chemical Engineering Journal*, *156*(1), 2–10. https://doi.org/10.1016/J.CEJ.2009.09.013

[39] Wang, J. & Guo, X. (2020). Adsorption kinetic models: Physical meanings, applications, and solving methods. *Journal of Hazardous Materials*, *20*, 1–20. https://doi.org/10.1016/j.jhazmat.2020.122156

[40] Lakrat, M., Azzaoui, K., Jodeh, S., Akartasse, N., Mejdoubi, E. & Lamhamdi, A. (2017). The removal of methyl orange by nanohydroxyapatite from aqueous solution : isotherm , kinetics and thermodynamics studies. *Desalination and Water Treatment*, *85*, 237–249. https://doi.org/10.5004/dwt.2017.21260

[41] Shah, S. S., Sharma, T., Dar, B. A. & Bamezai, R. (2021). Adsorptive removal of methyl orange dye from aqueous solution using populous leaves: Insights from kinetics, thermodynamics and computational studies. *Environmental Chemistry and Ecotoxicology*, *3*, 172–181. https://doi.org/https://doi.org/10.1016/j.enceco.2021.05.002.

[42] Sahoo, T. R. & Prelot, B. (2020). Adsorption processes for the removal of contaminants from wastewater: the perspective role of nanomaterials and nanotechnology. In *Nanomaterials for the Detection and Removal of Wastewater Pollutants*. Elsevier Inc. https://doi.org/10.1016/B978-0-12-818489-9.00007-4

[43] Abbas, F. S. (2013). Dyes removal from wastewater using agricultural waste. *Advances in Environmental Biology*, *7*(6), 1019–1026.

[44] Ding, W., Habineza, A., Zeng, X., Yan, Z., Yan, J. & Yang, G. (2022). Adsorption of Methylene blue and Methyl orange on nano zero-valent iron (nZVI) coated biochar: column adsorption experiments. *Desalination and Water Treatment*, *260*, 169–178. https://doi.org/https://doi.org/10.5004/dwt.2022.28445

[45] Ebelegi, A. N., Ayawei, N. & Wankasi, D. (2020). Interpretation of Adsorption Thermodynamics and Kinetics. *Open Journal of Physical Chemistry*, *10*(03), 166–182. https://doi.org/10.4236/ojpc.2020.103010

[46] Bouider, B. & Rida, K. (2022). Development of biomass activated carbon using full factorial design for the removal of methyl orange from aqueous solution. *Desalination and Water Treatment*, *267*, 240–252. https://doi.org/https://doi.org/10.5004/dwt.2022.28668

[47] Bahrouni, Y., Chouaieb, I., Kahri, H., Barhoumi, H. & Ayed, B. (2025). Enhanced methyl orange dye removal using a novel synthesized hybrid compound supported on activated charcoal. *Journal of Molecular Structure*, *1348*, 143432. https://doi.org/https://doi.org/10.1016/j.molstruc.2025.143432

[48] Cheng, T., Li, J., Ma, X., Zhou, L., Wu, H. & Yang, L. (2021). The adsorption properties of microporous activated carbon prepared from pistachio nut shell for low-concentration VOCs under low-medium temperatures. *Environmental Science and Pollution Research*, *28*(46), 65216–65228. https://doi.org/10.1007/s11356-021-14586-y

[49] Obradovic, B. (2020). Guidelines for general adsorption kinetics modeling. *Hemijska Industrija*, *74*(1), 65–70. https://doi.org/https://doi.org/10.2298/HEMIND200201006O 65

[50] Nkosinathi, D. G., Albertus, B. K., Jabulani, S. S. E., Siboniso Siphephelo, M. & Pullabhotla, R. V. (2020). Biosynthesis, Characterization, and Application of Iron Nanoparticles: in Dye Removal and as Antimicrobial Agent. *Water, Air, and Soil Pollution*, *231*(3), 1–10. https://doi.org/10.1007/s11270-020-04498-x.

[51] Rahman, M. L., Shamrih, S. A., Azlyzan, N. A., Sarjadi, M. S., Arsad, S. E., Sarkar, S. M. & Kumar, S. (2025). Removal of heavy metal ions from wastewater using modified cornstalk cellulose-derived poly(amidoxime) ligand. *Carbohydrate Polymer Technologies and Applications*, *9*, 100633. https://doi.org/10.1016/J.CARPTA.2024.100633

[52] Juturu, R., Ramachandra, V. & Selvaraj, R. (2024). Efficient adsorption of Cr (VI) onto hematite nanoparticles : ANN , ANFIS modelling , isotherm , kinetic , thermodynamic studies and mechanistic insights. *Chemosphere*, *349*(October 2023), 140731. https://doi.org/10.1016/j.chemosphere.2023.140731

[53] Muinde, V. M., Onyari, J. M., Wamalwa, B. & Wabomba, J. N. (2020). Environmental Chemistry and Ecotoxicology Adsorption of malachite green dye from aqueous solutions using mesoporous chitosan-zinc oxide composite material. *Environmental Chemistry and Ecotoxicology*, *2*, 115–125. https://doi.org/10.1016/j.enceco.2020.07.005

[54] Adekola, F. A., Hodonou, D. S. S. & Adegoke, H. I. (2016). Thermodynamic and kinetic studies of biosorption of iron and manganese from aqueous medium using rice husk ash. *Applied Water Science*, *6*(4), 319–330. https://doi.org/10.1007/s13201-014-0227-1

[55] Chong, Z. T., Soh, L. S. & Yong, W. F. (2023). Valorization of agriculture wastes as biosorbents for adsorption of emerging pollutants: Modification, remediation and industry application. *Results in Engineering*, *17*, 100960. https://doi.org/10.1016/J.RINENG.2023.100960

Appendix

Table 5: PAnalytical X'Pert Highscore interpretation of XRD in respect to FeNps synthesis at optimum condition

POS. [°2Θ.]	HEIGHT [CTS]	FWHM LEFT [2TH)	D-SPACING [Å]	REL. INT. [%]	TIP WIDTH	MATCHED BY
21.085290	41.074790	0.118080	4.21352	46.22	0.1417	00-001-0401
24.028480	17.711390	0.472320	3.70367	19.93	0.5668	01-073-0603
26.937920	88.862520	0.098400	3.30990	100.00	0.1181	
35.640420	19.058260	0.196800	2.51915	21.45	0.2362	01-073-0603
36.606860	21.510350	0.236160	2.45483	24.21	0.2834	00-001-0401
57.124630	2.298859	0.787200	1.61245	2.59	0.9446	01-073-0603

Table 6: PAnalytical X'Pert Highscore interpretation of XRD in respect to FeNps/MMS

POS. [2Θ.]	HEIGHT [CTS]	FWHM LEFT [2TH)	D-SPACING [Å]	REL. INT. [%]	TIP WIDTH	MATCHED BY
8.557138	7.233776	0.137760	10.33348	3.47	0.1653	
11.018830	1.560303	0.787200	8.02981	0.75	0.9446	
24.263200	29.731810	0.236160	3.66837	14.26	0.2834	01-073-0603
26.873070	208.442200	0.157440	3.31774	100.00	0.1889	
35.549940	23.926820	0.236160	2.52535	11.48	0.2834	01-073-0603
67.973820	34.826120	0.118080	1.37913	16.71	0.1417	

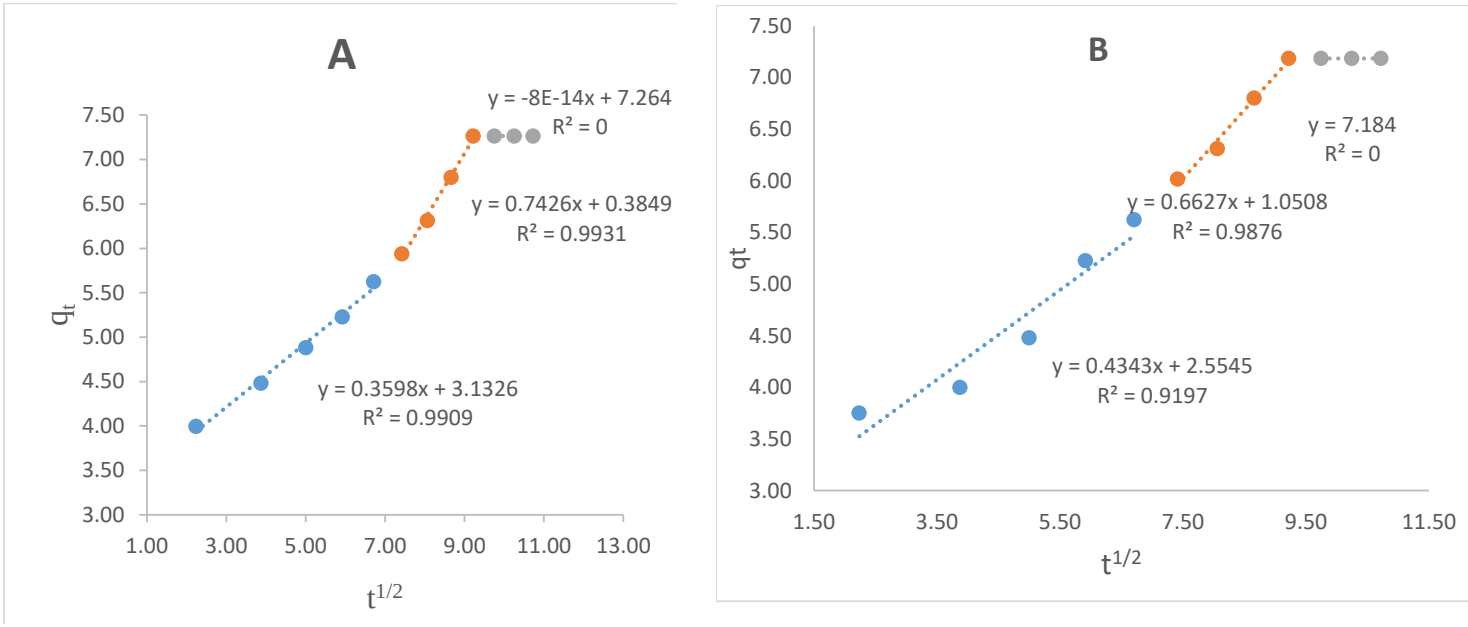

Figure 8: Multi-layer intraparticle analysis for CR (A) and MO (B) on FeNPs/MMS